Estimation of curl in paper: An industrial application combining shape measurement and least squares modeling

Tomas Berglund[a] and Per Synnergren[b] and Inge Söderkvist[c]

[a]Division of Computer Science, Luleå University of Technology, S-971 87 Luleå, Sweden
[b]Division of Experimental Mechanics, Luleå University of Technology, S-971 87 Luleå, Sweden
[c]Department of Mathematics, Luleå University of Technology, S-971 87 Luleå, Sweden

ABSTRACT

If a sheet of paper is subjected to humidity changes and have structural variations through its thickness such as gradients of fibre orientation, density and filler content, the sheet will curl and hence assume a cylindrical shape. Curl is a quality problem that makes the paper less suitable for printing. We propose a method to measure curl that can be used for automated analysis of the paper quality. The shape of the curled paper is measured from the perspective difference in a stereoscopic camera system, which is viewing an irregular pattern that is projected onto the specimen. The perspective difference is calculated by a correlation algorithm, a technique often referred to as digital speckle photography. The most interesting quality parameters are the magnitude of curl, which is defined as the inverse of the radius of curvature and also the orientation of the curled paper. These parameters are estimated by performing a least squares fit of a cylindrical shape to the three-dimensional measurement data. The least-squares model is nonlinear and an iterative technique based on the Gauss-Newton algorithm is used. In addition to a description of our methods we also present experimental results that illustrate their performance.

Keywords: Shape measurements, Digital Speckle Photography, Nonlinear least squares fitting, Paper curl estimation

1. INTRODUCTION

During the last decade, increased production rates and reduced tolerances in printing have increased the quality demands on paper and board. This has pushed the paper manufacturers to learn more about, and improve their products, in order to prevent costly claims from customers. One of the main problems is curl. Curl is defined as the global curvature of a sheet of paper caused by ambient humidity changes. Any paper with structural variations through its thickness, such as gradients of fibre orientation, density and filler content will curl upon humidity changes. Humidity changes that for instance occurs during the printing process. Due to the economic significance of the curl problem, much work has been done to investigate sheet design and processing strategies to reduce such problems. Although, the causes of curl are well documented, there are complexities such as history-dependent material properties and geometrical nonlinearities that are still under investigation. Several researchers have worked in this field, for some examples see Ref. 1–5.

Commonly, a curled paper sheet takes the shape of a cylinder with the symmetry axis along of the direction of the minimum hygroexpansion and maximum stiffness.[6,7] This is usually very close to the direction of manufacture, which is referred to as machine direction (MD). Thus, the most interesting quality parameters are the radius of curvature and the orientation of the curled paper compared to the machine direction. Nordström et al. estimated these parameters by performing a least squares fit of a second order polynomial to the surface profile data captured by laser scanning triangulation.[8] Although optical methods have been used to measure curl, the standardized method, defined in ISO 11556:1998, is to use a vernier calliper.

Whole-field surface profile measurements by non-contact optical methods have been extensively studied because of their importance in automated manufacturing, quality control and robotics.[9–12] Most often periodic patterns,

Further author information: (Send correspondence to P.S)
T.B: E-mail: Tomas.Berglund@sm.luth.se
P.S.: E-mail: Per.Synnergren@mt.luth.se
I.S.: E-mail: Inge.Soderkvist@sm.luth.se

such as parallel fringes, are projected onto the object surface either by conventional white-light imaging system or coherent light interference patterns. The image of the parallel fringes, which is generally acquired with a CCD-camera, becomes deformed by the surface, so that the phase distribution includes information of the surface profile. By extracting the phase distribution of the fringes quantitative analysis of the shape can be carried out. Methods based on the Fourier transform method[11] or by phase stepping[12] of the fringe pattern are commonly used to do this. The result from such measurements will appear as wrapped phase maps (i.e., phase lying in the range $-\pi$ to π). These phase maps have to be unwrapped for the actual shape of the object to be found. However, phase unwrapping can turn out to be impossible when the technique is applied to real engineering objects since such objects often contains sudden jumps (discontinuities) in the profile. One solution to the unwrapping problem is to use the concept of temporal phase unwrapping,[13] which means that a time sequence of parallel fringes with a different pitch is projected onto the object. The phase at each pixel is then unwrapped along the time axis independently from all other pixels. Thus, the position in space for each pixel can be determined uniquely and the shape of the object is found.

Another solution to the discontinuity problem is to use a random pattern instead of repetitive fringes.[14] A random pattern varies randomly, so that every little sub-area of the pattern becomes unique. In this case the phase distribution carries no useful information and can not be used. The solution is to capture the random pattern in two different states. One way is to acquire a reference image when the random pattern is projected onto a flat reference plate. Replacing the flat plate with the object of interest, the random pattern will move onto the CCD-detector. By following the motion of each specific sub-area of the image, the shape of a discontinuous object can be determined. A slightly different method is to measure shape by using the perspective difference in a stereoscopic camera system. Two cameras are viewing a random pattern that is projected onto the surface of the specimen. The different positions of the cameras and the varying height of the specimen will make the acquired images of the pattern slightly different. By analyzing the image pair, with a cross-correlation technique (a technique often referred to as digital speckle photography (DSP)[15]), a displacement field that is proportional to the object shape will be obtained.

In this paper we propose a method to measure curl by using the DSP technique combined with a stereo imaging system (stereo-DSP).[16] A Fibro DST1230 system was used. This apparatus is developed in a co-operation between Fibro Systems AB and the Division of Experimental Mechanics, Luleå University of Technology. It is originally built to test the dynamic stability in paper by measuring the 3-D surface displacement field that occurs during changes in humidity or heating. This work was performed to broaden the applicability of the system by using its shape measuring capabilities combined with nonlinear least squares techniques for fitting of a model of a half-cylinder to estimate curl.

Least squares fitting is widely used in experimental sciences because of its nice statistical and computational properties.[17,18] Most often a model that depends linearly on some unknown parameters is fitted to some measurements. However, in many cases it is possible to obtain a more accurate model by allowing the model to depend nonlinearly on the parameters. The curled paper has shown to be accurately approximated using a nonlinear half-cylinder model. The parameters that determine the shape, orientation, and position of the cylinder are found using the iterative Gauss-Newton algorithm.[18] The iteration needs good initial values on the unknown parameters. Those values are obtained by fitting a quadratic surface to the measurements using a linear least squares technique.

In addition to a description of our methods we also present experimental results that illustrate their performance.

2. SHAPE MEASUREMENTS

Consider the optical arrangement shown in Fig. 1. A random intensity distribution was projected on the object surface by letting white light passing through a glass plate with a random transmission function distribution. The glass plate was in fact a developed photographic plate, which imaged a laser speckle pattern. Image pairs of the object of interest covered with the projected pattern were acquired by two CCD-cameras that formed a stereovision set-up. Stereovision was achieved by the so-called translated lens method.[16] This means that the cameras are aligned so that their detectors and lens planes are all in parallel and the optical axis of the lenses are moved sideways from the centre of the active CCD area. Because of that the optical axes are in parallel, a perfectly aligned translated lens set-up have the advantage that the cameras can be adjusted so that their focus planes coincide in space. Thus, if the focus depth of the cameras is greater than the depth of the object, it is easy to obtain object images that are well focused across the image plane for both cameras simultaneously.

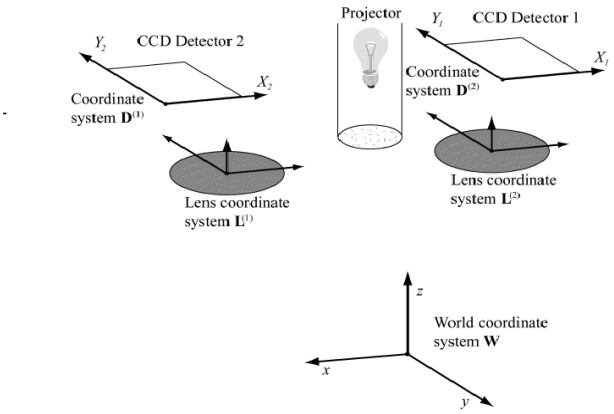

Figure 1. A schematic of the optical system. It consists of two CCD-cameras and a white-light projector and shows five coordinate systems, namely $\mathbf{L}^{(1)}$, $\mathbf{L}^{(2)}$, $\mathbf{D}^{(1)}$, $\mathbf{D}^{(2)}$ and $\mathbf{W}$.

Five coordinate systems are used to relate points on the object with corresponding points in the images, see Fig. 1. The orientations of the lens coordinate systems $\mathbf{L}^{(1)}$, $\mathbf{L}^{(2)}$ and of the detector coordinate systems $\mathbf{D}^{(1)}$, $\mathbf{D}^{(2)}$, are related to the orientation of the world coordinate systems, $\mathbf{W}$, by rotation matrices $R_L^{(i)}, R_D^{(i)}, i = 1, 2$. For a reasonable well built translated lens system, the rotations between the systems are small. Hence, we use the trigonometric approximations $\cos(\phi) \approx 1$, and $\sin(\phi) \approx \phi$ and approximates the rotation matrices as

$$R_L^{(i)} \approx \begin{bmatrix} -1 & 0 & \alpha_2^{(i)} \\ 0 & -1 & -\alpha_1^{(i)} \\ \alpha_2^{(i)} & -\alpha_1^{(i)} & 1 \end{bmatrix} \quad \text{and} \quad R_D^{(i)} \approx \begin{bmatrix} 1 & \beta_3^{(i)} & \beta_2^{(i)} \\ \beta_3^{(i)} & 1 & -\beta_1^{(i)} \\ \beta_2^{(i)} & -\beta_1^{(i)} & 1 \end{bmatrix}, \; i = 1, 2. \tag{1}$$

The coordinate system $\mathbf{L}^{(i)}$, which originally was aligned with $\mathbf{W}$, has been rotated by angles $\alpha_1^{(i)}, \alpha_2^{(i)}$ and π around respective coordinate axis. The angles $\beta_1^{(i)}, \beta_2^{(i)}$ and $\beta_3^{(i)}$ determine the corresponding rotations of detector coordinate system $\mathbf{D}^{(i)}$ around the axes of system $\mathbf{L}^{(i)}$.

Let the origin of $\mathbf{W}$ and the origin of $\mathbf{D}^{(i)}$ be expressed, in the lens coordinate system $\mathbf{L}^{(i)}$, by the vectors $\mathbf{o}^{(i)}$ and $\mathbf{c}^{(i)} = (c_1^{(i)}, c_2^{(i)}, c_3^{(i)})$, respectively. Further more, we introduce the points $\tilde{\mathbf{p}}^{(i)} = (\tilde{x}^{(i)}, \tilde{y}^{(i)}, \tilde{z}^{(i)}) = \mathbf{p} + \mathbf{o}^{(i)}$, $i = 1, 2$, as translations of a point $\mathbf{p} = (x, y, z)$ given in world coordinates. It can then be shown that the relationship between detector positions $(X^{(i)}, Y^{(i)})$, $i = 1, 2$, with a corresponding point $\mathbf{p}$ expressed in world coordinates, for the translated lens method, is given by the following equations[16];

$$X = h_X(x, y, z) = c_1 + \beta_3 c_2 + \frac{\tilde{x}(\beta_2 c_1 - \beta_1 c_2 + c_3) + \tilde{y}\beta_3 c_3 - c_3\alpha_2 z}{\tilde{z}} + \frac{c_3\tilde{x}}{\tilde{z}^2}\Phi, \tag{2}$$

$$Y = h_Y(x, y, z) = -\beta_3 c_1 + c_2 + \frac{\tilde{y}(\beta_2 c_1 - \beta_1 c_2 + c_3) - \tilde{x}\beta_3 c_3 + c_3\alpha_1 z}{\tilde{z}} + \frac{c_3\tilde{y}}{\tilde{z}^2}\Phi, \tag{3}$$

where we for simplicity have dropped the camera index $^{(i)}$ and where Φ is defined, using the focal length, f, and the distortion factor, Ψ, of the camera lenses, as

$$\Phi = \beta_2\tilde{x} - \beta_1\tilde{y} - \alpha_2 x + \alpha_1 y + \frac{\Psi}{f + \tilde{z}}(\tilde{x}^2 + \tilde{y}^2).$$

Hence, in order to get the world coordinates of a point on the object surface, given the corresponding detector coordinates, the system must be calibrated, i.e., the positions of the cameras relative the measurement volume, misalignments (the small rotation) and the effect of distortion in the images must be known. The calibration routine used is described in Ref. 16.

An image pair of the speckle-covered specimen is captured. The images are called $I^{(1)}$ and $I^{(2)}$, where the index denotes from which camera the image originate. Correlating a field of small sub-images from $I^{(1)}$ with $I^{(2)}$ using the

DSP-algorithm[15] gives the detector positions, $(X^{(1)}, Y^{(1)})$ and $(X^{(2)}, Y^{(2)})$, for corresponding position of the object surface. The results of the cross-correlation can be written as $dX = X^{(1)} - X^{(2)}$ and $dY = Y^{(1)} - Y^{(2)}$. Thus, using (2) and (3), with camera index $i = 1, 2$ we obtain a set of four equations

$$\begin{cases} X^{(1)} = h_X^{(1)}(x, y, z) \\ X^{(2)} = X^{(1)} + dX = h_X^{(2)}(x, y, z) \\ Y^{(1)} = h_Y^{(1)}(x, y, z) \\ Y^{(2)} = Y^{(1)} + dY = h_Y^{(2)}(x, y, z) \end{cases} \tag{4}$$

with only three unknowns (x, y, z). However, this overdetermined system of equations is not easily solved analytically. Therefore an iteration procedure based on fixed point iteration, followed by an averaging technique, is used. By neglecting the influence of distortion and the small rotations, an exact analytic solution can be found. This solution provides a good approximation of the shape of the object surface and is used as start values in the iterative process. If good quality lenses are used, the effect of distortions and misalignments are rather small and varies slowly due to small differences of the object point position. Thus, the iteration converges fast.

3. FITTING OF A HALF-CYLINDER MODEL

3.1. A Cylinder Model

Let (x', y', z') denote the coordinates of a point expressed in an orthogonal coordinate system $\mathbf{W}'$ with axes $(\mathbf{x}', \mathbf{y}', \mathbf{z}')$. Furthermore, assume that there is a cylinder in $\mathbf{W}'$ having $\mathbf{y}'$ as its central axis. The upper half $(z' >= 0)$, of the cylinder can, in the system $\mathbf{W}'$, be written as

$$z'(x', y') = \sqrt{r^2 - x'^2} \tag{5}$$

where r is the radius, $-r \leq x' \leq r$ and $-\infty \leq y' \leq \infty$.

Let (x, y, z) denote the coordinates of a point expressed in the orthogonal world-coordinate system $\mathbf{W}$. The measurement technique provides a set of world-coordinates, $\{(x_j, y_j, z_j),\ j = 1, \ldots, m\}$, of points on the surface of the curled paper. Thus we can fit a half-cylinder to the measurements by determining the shape parameter r as well as the transformation between the coordinate systems $\mathbf{W}$ and $\mathbf{W}'$ that describes the orientation and position of the cylinder. The transformation between the coordinate systems can be written as

$$\begin{pmatrix} x \\ y \\ z \end{pmatrix} = \begin{bmatrix} \cos(\theta_z) & -\sin(\theta_z) & 0 \\ \sin(\theta_z) & \cos(\theta_z) & 0 \\ 0 & 0 & 1 \end{bmatrix} \begin{bmatrix} 1 & 0 & 0 \\ 0 & \cos(\theta_x) & -\sin(\theta_x) \\ 0 & \sin(\theta_x) & \cos(\theta_x) \end{bmatrix} \left(\begin{pmatrix} x' \\ y' \\ z' \end{pmatrix} + \begin{pmatrix} a_x \\ 0 \\ a_z \end{pmatrix} \right). \tag{6}$$

By substituting (5) into (6) we can express z as

$$z = g(\mathbf{u}, x, y) = \tan(\theta_x)\,(y\cos(\theta_z) - x\sin(\theta_z)) + \frac{\sqrt{r^2 - (y\sin(\theta_z) + x\cos(\theta_z) - a_x)^2} + a_z}{\cos(\theta_x)} \tag{7}$$

where $g(\mathbf{u}, x, y)$ is a function that depends nonlinearly of the unknown half-cylinder parameters that are stacked into the column vector $\mathbf{u} = (r, \theta_x, \theta_z, a_x, a_z)^t$.

3.2. The Gauss-Newton Algorithm

Since the measurement errors occur mostly in the z-coordinates it makes sense to fit a half-cylinder to the measurements by solving the nonlinear least squares problem

$$\min_{\mathbf{u} \in \mathbf{R}^5} \sum_{j=1}^{m} (g(\mathbf{u}, x_j, y_j) - z_j)^2. \tag{8}$$

The Gauss-Newton algorithm that is used for solving this problem belongs to the family of "search direction algorithms" that solves nonlinear minimization problems using the iteration

$$\mathbf{u}^{(k+1)} = \mathbf{u}^{(k)} + \alpha^{(k)}\,\mathbf{p}^{(k)}, \tag{9}$$

where k is an iteration index, $\mathbf{p}^{(k)}$ is a search direction, and $\alpha^{(k)}$ is a step length (damping factor) that is used to assure convergence. Gauss-Newtons method computes the search direction by solving the linear least squares problem

$$\min_{\mathbf{p}} \|J^{(k)}\mathbf{p}^{(k)} - \mathbf{e}^{(k)}\|_2, \tag{10}$$

where $J^{(k)} \in R^{m\times 5}$ is a Jacobian matrix with its j:th row equal to the gradient $\partial g/\partial \mathbf{u}(\mathbf{u}^{(k)}, x_j, y_j)$, and $\mathbf{e}^{(k)} \in R^m$ is a column vector with its j:th element, $e_j^{(k)}$, equal to $g(\mathbf{u}^{(k)}, x_j, y_j) - z_j$. In our implementation we have used a step length computed using the Armijo-Goldstein condition, see Ref. 18 for details.

3.3. Finding Initial Parameter Values

The iterative scheme described above needs an initial value $\mathbf{u}^{(0)}$ of the parameters that describe the half-cylinder. Similar to the method used by Nordström et al.[8] we fit a quadratic surface

$$z = q(x, y) = k_0 + k_1 x + k_2 y + k_3 x^2 + k_4 y^2 + k_5 xy, \tag{11}$$

to the measurements using a linear least squares technique. From this model we extract curvature information that describes both the orientation of the half-cylinder and its radius.

Let $\nabla q = (q_x, q_y)^t$ denote the gradient of the quadratic function $q(x, y)$ evaluated at a point $(\hat{x}, \hat{y})$. The tangent plane of the quadratic surface at the point $(\hat{x}, \hat{y})$ is spanned by the vectors $\mathbf{t_1} = (1,\ 0,\ q_x)^t$ and $\mathbf{t_2} = (0,\ 1,\ q_y)^t$, and has the vector $\mathbf{n} = (-q_x,\ -q_y,\ 1)^t/\sqrt{(q_x^2 + q_y^2 + 1)}$ as a unit normal. Introducing the matrices $T \in R^{3\times 2}$ with columns $\mathbf{t_1}$ and $\mathbf{t_2}$, the Hessian matrix $\nabla^2 q(\hat{x}, \hat{y}) \in R^{2\times 2}$, and the matrix $H = \nabla^2 q(\hat{x}, \hat{y})/\sqrt{(q_x^2 + q_y^2 + 1)}$, the normal curvature at $(\hat{x}, \hat{y})$ in the tangent direction $T\mathbf{v}$ is defined as[19]

$$\kappa = \frac{\mathbf{v}^t H \mathbf{v}}{\mathbf{v}^t T^t T \mathbf{v}}. \tag{12}$$

The normal curvature measures how much the direction of the normal changes when we move in direction $T\mathbf{v}$. The principal directions that gives the largest and smallest normal curvature can easily be obtained by solving the generalized (2×2) eigenvalue problem

$$H\mathbf{v} = T^t T \mathbf{v}\lambda. \tag{13}$$

The initial value of the radius of the half-cylinder is approximated by the reciprocal of the largest curvature of the quadratic surface, i.e., $r^{(0)} = 1/\max(\lambda_1, \lambda_2)$.

Let $\mathbf{v}_1$ denote the eigenvector associated to the smallest curvature. The initial value $\theta_z^{(0)}$ of the angle θ_z, is then computed as the angle between $\mathbf{v}_1$ and the $\mathbf{y}$-axis. The initial value $\theta_x^{(0)}$ of the angle θ_x, is computed as the angle between $(0, 1, dz)^t$ and the $\mathbf{y}$-axis, where $dz = \mathbf{v}_1^t \nabla q$ is the directional derivative of the quadratic function along direction $\mathbf{v}_1$.

To find the initial values $a_x^{(0)}$ and $a_z^{(0)}$ of the translation parameters a_x and a_z we use that the $x-$ and $y-$ coordinates of the measurements $\{(x_j, y_j, z_j),\ j = 1, .., m\}$ are almost uniformly distributed. We also assume that the measurements correspond to a curled paper that is almost centered in the apparatus. The point of evaluation, $(\hat{x}, \hat{y})$, is chosen as the mean values $\hat{y} = \overline{y}$ and $\hat{x} = \overline{x}$ and implies that the point $(\hat{x}, \hat{y}, q(\hat{x}, \hat{y}))^t$ is close to the top of the half-cylinder, i.e., $\hat{x}$ corresponds to $x' \approx 0$ in $\mathbf{W}'$. Hence, we set $x' = 0$ and use $x = \hat{x}$, $y = \hat{y}$, $z = q(\hat{x}, \hat{y})$ together with (6) and the previously evaluated initial values to get

$$a_x^{(0)} = \cos(\theta_z^{(0)})\hat{x} + \sin(\theta_z^{(0)})\hat{y}, \tag{14}$$

$$a_z^{(0)} = \sin(\theta_z^{(0)})\sin(\theta_x^{(0)})\hat{x} - \cos(\theta_z^{(0)})\sin(\theta_x^{(0)})\hat{y} + \cos(\theta_x^{(0)})z(\hat{x}, \hat{y}) - r^{(0)}. \tag{15}$$

3.4. The Use of Weights

The measurement technique, see Sect. 2, provides a measure, $0 < \delta_j < 1$, of the correlation between the two detected speckle projections corresponding to the j:th measurement point, $j = 1, \ldots, m$. It can be shown, see Ref. 20, that $\mathcal{C}_j = \sqrt{(1 - \delta_j)/\delta_j}$ is approximately proportional to the standard deviation of the error in the j:th measurement point. That makes it possible to define weights, $w_j = 1/\mathcal{C}_j$, $j = 1, \ldots, m$, that correspond to the relative accuracy

Figure 2. A photograph of the experimental set-up (Fibro DST1230 system) used in the investigation.

of each measurement. The weights are incorporated into the fitting model by solving the weighted nonlinear least squares problem

$$\min_{\mathbf{u}} \sum_{j=1}^{m} (w_j(g(\mathbf{u}, x_j, y_j) - z_j))^2, \tag{16}$$

instead of problem (8). If the the difference in magnitude between the weights is large we get an ill-conditioned problem and particular considerations may be needed to accurately solve the problem.[21] This is not the case here and the weighted problem is solved using the same technique, based on (9) and (10), as for the nonweighted case. The only differences is that the j:th row of the Jacobian, $J^{(k)}$, becomes $w_j \partial g / \partial \mathbf{u}(\mathbf{u}^{(k)}, x_j, y_j)$ and that the j:th element of the residual vector $\mathbf{e}^{(k)}$ becomes $w_j(g(\mathbf{u}^{(k)}, x_j, y_j) - z_j)$.

4. EXPERIMENTAL RESULTS

All together six experiments have been performed in order to validate the usability of our method. General information about the experiments and basics of the presented results are given in Section 4.1. Sect. 4.2 contains results of four experiments where we have applied the method on a cylindrical object. Section 4.3 shows results from measurements of curled paper.

4.1. General Information

The experimental set-up used is shown in Fig. 2. The rig is built by FIBRO Systems AB. It is originally designed for measurements of 3-D deformations (or dynamic stability testing) of copy paper subjected to humidity or temperature changes. Two SONY XC-77 ce cameras with synchronous pixel clocking are used. The cameras are connected to a PC through a Leutron Vision Picport Stereo H4S framegrabber, enabling images of 512×512 pixels to be captured. The focal length of the lenses is 35 mm. Two different types of specimens were used namely apiece of a cylindrical waste-pipe that was split into a half-cylinder and paper specimens that were made out of ordinary copy paper. The radius of the waste-pipe was measured to 77.7 mm by using a calliper. The waste-pipe was mounted on a polarizer holder that served as a rotational stage. The paper specimens were cut as round discs and they were forced to curl by applying moisture from a water spray can. The lack of a proper humidity chamber lead to problems measuring the curl of the papers manually as the curl becomes time dependent. Therefore only the computed estimates of the paper curl are presented. Note that curl is defined as the inverse of the radius, r, with a dimension of m^{-1}. We, however, only presents the estimates of the radii.

Case	r	θ_x (°)	θ_z (°)	a_x	a_z	m (no.)	$\overline{\lvert e \rvert}$	max($\lvert e \rvert$)	s
1	77.6595	1.4317	0.79367	58.3912	−40.0365	570	0.14864	2.1307	0.26371
2	**77.6376**	**1.48**	**30.8041**	**82.8426**	**−39.0901**	**525**	**0.13285**	**1.2827**	**0.21887**
3	77.7937	1.519	45.846	86.9251	−38.6799	533	0.12335	1.4604	0.20725
4	77.6171	−1.6697	−89.2858	−64.4722	−36.6985	513	0.089029	0.9281	0.14327

Table 1. The results from the fitting of a half-cylinder rotated $\theta_{z_1} \approx 0°$, $\theta_{z_2} \approx 30°$, $\theta_{z_3} \approx 45°$ and $\theta_{z_4} \approx 90°$ corresponding to the four different cases of the table. The radius r was measured manually to 77.7 mm. The unit is millimeter (mm) for all entries except from the angles θ_x and θ_z, which are given in degrees (°), and the number of measurements m, which is a natural number. The bold-face row corresponds to the half-cylinder treated in Fig. 3 and Fig. 4.

The original shape measurements were filtered to guarantee that all data points originates from the object of interest and to discard noisy sample points. The filtering algorithm used was simple. First, in order to only consider accurate measurements, we used constraints $\delta_j > 0.8$, $j = 1, \ldots, m$, on the correlation measures. Secondly, if the paper has extensive curl, the specimen might not cover the whole image-field of the cameras. Then some of the measured z-values will originate from parts of the set-up rather than the specimen. Due to the geometry of the set-up such data has z-values near 0 mm. These data points must be filtered away or they might introduce errors in the surface fitting, therefore data with low z-values are discarded.

In order to have estimates of the accuracy of the method we let $\mathbf{u}^*$ denote the computed solution of (16). Then we let the error or residual, e_j, of the j:th measurement be defined by $e_j = g(\mathbf{u}^*, x_j, y_j) - z_j$, $j = 1, \ldots, m$. We let the mean error, $\overline{e}$, and the mean absolute error, $\overline{|e|}$, be defined by $\overline{e} = \frac{1}{m}\sum_{j=1}^{m} e_j$ and $\overline{|e|} = \frac{1}{m}\sum_{j=1}^{m} |e_j|$ respectively. Furthermore we let the maximum absolute error and the standard deviation of e_j, $j = 1, \ldots, m$, be denoted max($|e|$) and s respectively. The above errors consist of model errors as well as errors in the surface profile measurements. If we assume that the standard deviation is taken to be an estimate of the random error in the shape measurement, the expected random error can be written as $s_{\text{shape}} = k\sqrt{(1-\delta)/\delta}$.[20] The constant k depends on the geometry of the optical set-up, the speckle size in the projected pattern and the sub-image size used. The correlation δ is an output from the DSP-algorithm. The value of k was found from an experiment, in which the shape of a reference flat was measured. The random error in that particular measurement was estimated by calculating the standard deviation from a plane, which was fitted to the surface profile data. The mean correlation was $\delta = 0.984$ and the random error was $s_{\text{shape}} = 0.062$ mm, which gives $k = 0.486$ mm.

The damping of the Gauss-Newton method never came in hand during the estimations. Numerical experiments indicate that the initial values on the unknown parameters are so close to optimal that $\alpha^{(k)} = 1$ at all iterations is a possible alternative.

4.2. Validation of the Technique

A set of four measurements (Case 1, 2, 3 and 4) of the waste pipe was performed to test the validity of the technique. The waste pipe was rotated approximately $\theta_{z_1} \approx 0°$, $\theta_{z_2} \approx 30°$, $\theta_{z_3} \approx 45°$ and $\theta_{z_4} \approx 90°$ in the four measurements, respectively. The rotation was done with a manual rotation table having a resolution of 1° but not having a physical connection to the axes of the cameras. This means that the angles 30°, 45°, and 90° are only relative to the position of the half-cylinder in the first measurement.

The result from the four measurements are shown in Table 1, in which parameters of the fitted cylinder as well as estimates of the accuracy of the result are presented. Case 2 is bold-faced to indicate that this particular estimation is visualized as a plot of the measurement and as a histogram of the residuals in Fig. 3. In order to visualize the goodness of fit we have shown four projections of the model and the measurements of the half-cylinder in Fig. 4. The dots mark the measured data, the solid line is the model and the division into regions a), b), c) and d) is done according to Fig. 5. Note that Case 4 differs from the other cases in the respect that it has negative θ_z- and a_x-values. This is due to the non-unique parametrization of the half-cylinder orientation.

The mean correlation value, δ, for the four measurements ranged between 0.943 to 0.949. Hence the random error, s_{shape}, in the shape measurements of the waste pipe was expected to be in the interval 0.11 mm to 0.12 mm.

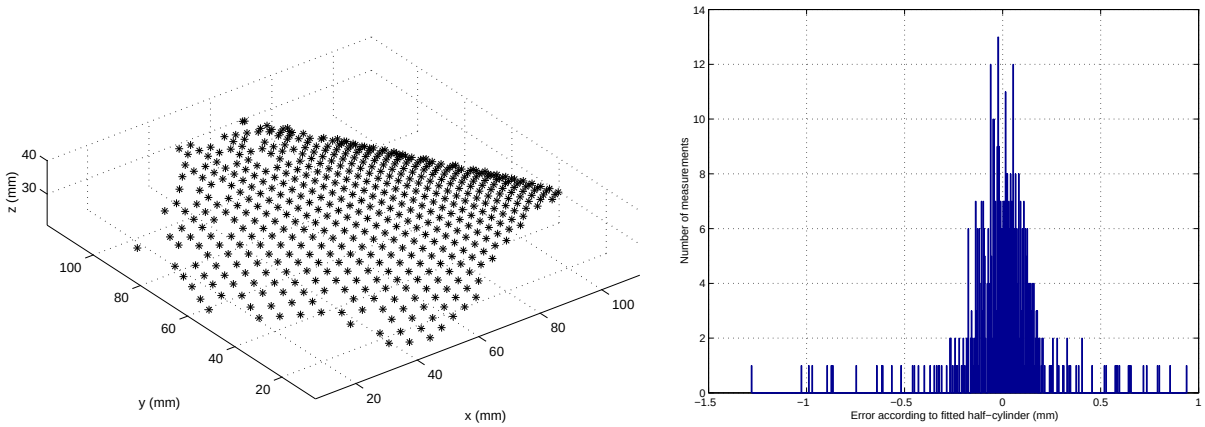

Figure 3. Two subplots of the Case 2 half-cylinder in Table 1 and Fig. 4. The left subplot shows measurements (dots) in (x, y, z) while the right subplot shows a histogram of the errors, e_j, $j = 1, \ldots, 525$, between the model and the measurements. The number of measurements is given on the vertical axis of the histogram while the errors are shown on the horizontal axis.

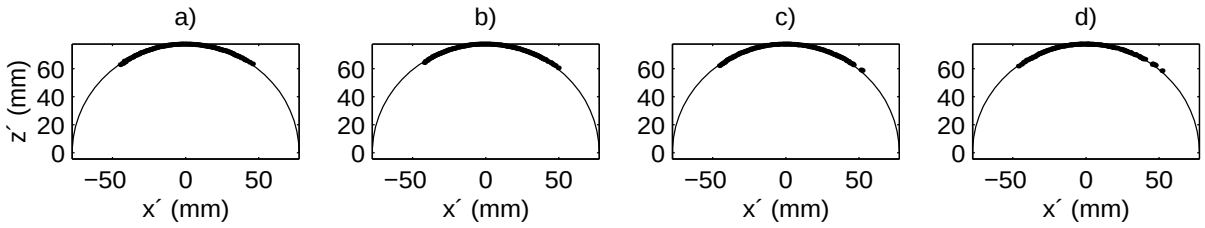

Figure 4. Projections on $y' = 0$ of the model (solid) and the measurements (dots) of the Case 2 half-cylinder in Table 1 and Fig. 3. The division into regions a), b), c) and d) along $\mathbf{y}'$ is the same as in Fig. 5.

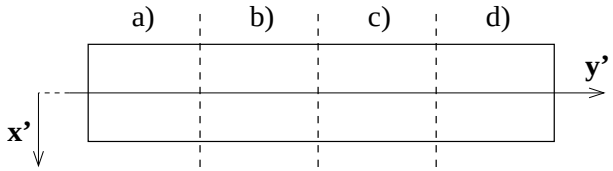

Figure 5. Schematic of how the four regions of measurements are built in Fig. 4 and Fig. 7. Each of the regions a), b), c) and d) along $\mathbf{y}'$ contain approximately 25% of the measurements. All together the regions contain all measurements.

Paper	r	θ_x (°)	θ_z (°)	a_x	a_z	m (no.)	$\overline{\lvert e \rvert}$	max($\lvert e \rvert$)	s
1	38.7865	1.4497	0.83556	58.346	9.9577	347	0.15439	3.0344	0.26212
2	**81.2783**	**0.764**	**1.9721**	**67.4229**	**−31.4288**	**615**	**0.5294**	**3.7891**	**0.77344**

Table 2. The results from the fitting of two curled papers. The unit is millimeter (mm) for all entries except from the angles θ_x and θ_z, which are given in degrees (°), and the number of measurements m, which is a natural number. The bold-face row corresponds to the curled paper treated in Fig. 6 and Fig. 7.

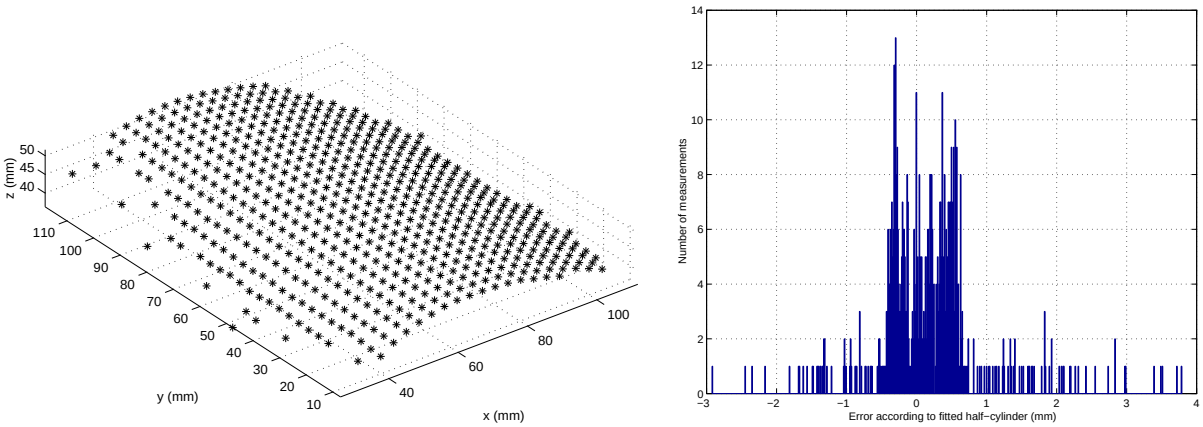

Figure 6. Two subplots of Paper 2 in Table 2 and Fig. 7. The left subplot shows measurements (dots) in (x, y, z) while the right subplot shows a histogram of the errors, e_j, $j = 1, \ldots, 615$, between the model and the measurements. The number of measurements is given on the vertical axis of the histogram while the errors are shown on the horizontal axis.

This is of the same order of magnitude as the standard deviation, s, of the residuals from the cylinder model, which was ranging from 0.14 mm to 0.26 mm. The mean value of the radius was calculated to $r = 77.68$ mm from the four cases in Table 1. This result shows good resemblance with the manually measured radius of $r = 77.7$ mm. We can also see that the difference between the smallest and largest estimation of r was less than 0.18 mm, which indicates that this method gives reliable and stable results. The standard deviation of the four estimations of the radius was 0.08 mm. The measured rotations from the first position of the waste pipe were 30.01°, 45.05° and 89.92°. This can be compared to the expected values of 30°, 45° and 90°, thus the difference between the measured and expected values are much smaller than the resolution of the rotational stage used. It can be concluded that we have good reasons to believe that the accuracy of this method is sufficient for the proposed application.

4.3. Estimation of Paper Curl

A set of two measurements (Paper 1 and 2) were performed on curled paper. The results of the two paper measurements are shown in Table 2. Parameters of the fitted half-cylinders as well as estimations of the accuracy of the result are found in the table. Paper 2 is bold-faced to indicate that the particular estimation is visualized in Fig. 6 and Fig. 7.

The random errors, s_{shape}, were estimated to 0.11 mm ($\delta = 0.951$) and 0.12 mm ($\delta = 0.940$) for Paper 1 and Paper 2 respectively. The estimates $\overline{|e|}$, max($|e|$) and s of Paper 1 are of equal magnitude as for the measurements on the waste-pipe. From experiments we found that a paper of high curl seem to be more cylindrical than a paper of low curl. The higher s and $\overline{|e|}$ of the Paper 2 estimate certainly comes from the fact that the model does not describe Paper 2 properly. This can be seen in Fig. 7 where the paper does not seem to have a half-cylindrical shape. Instead, it seems to be a little bit skewed. Despite this, most of the data is less than 1 mm from the model assumption, which indicates that the method can be used to estimate the parameters of curled paper with a high accuracy.

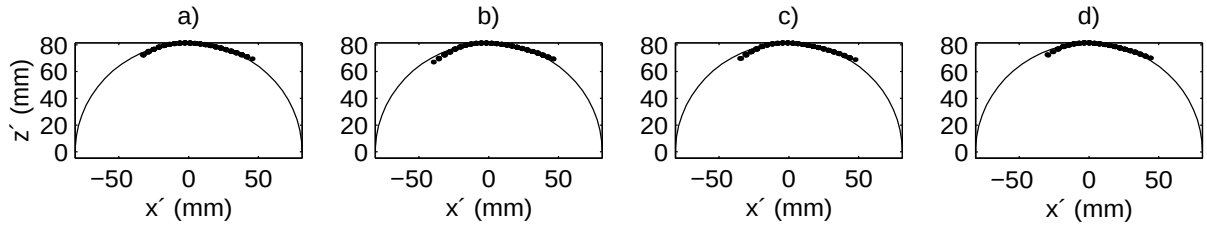

Figure 7. Projections on $y' = 0$ of the model (solid) and the measurements (dots) of Paper 2 in Table 2 and Fig. 6. The division into regions a), b), c) and d) along $\mathbf{y}'$ is the same as in Fig. 5.

5. CONCLUSIONS

It has been shown that curl in paper can be measured by combining optical shape measurement methods and least squares fitting. Research in paper mechanics has shown that a cylinder model accurately approximates the curled paper. Two parameters are of interest. One is called the magnitude of curl and is defined as the inverse of the radius of the fitted cylinder and the second is the orientation of the symmetry (curl) axis of the cylinder. Where the magnitude of curl gives an indication about how well the paper retains its original dimensions during changes in temperature and humidity. The shape of the curled paper is measured by using stereo-DSP. Surface profile measurements by optical methods is, however, an extensively studied field and several other methods like laser scanning triangulation and different types of fringe projection approaches could also successfully have been used. One advantage with the stereo-DSP approach is that the accuracy of each measured data point can be estimated. Thus, weights can be applied to the measured result, which guarantees a uniform standard deviation in the surface fitting. The parameters that determine the shape and orientation of the cylinder approximation of the curled paper are found by using an iterative Gauss-Newton algorithm.

Four measurements on a cylindrical waste pipe were performed to test the validity of the technique. The random errors, e.g. the standard deviation, in the shape measurements were estimated to be approximately 0.1 mm in all four cases. The standard deviation of the error from the cylindrical model was ranging from 0.14 mm to 0.26 mm. The radius of the waste pipe was calculated to 77.68 mm with a standard deviation of 0.08 mm. This can be compared with measurements performed with a vernier caliper that gives a radius of 77.7 mm. The waste pipe was mounted on a rotational stage and rotated 30°, 45° and 90° from its original position. The measured rotations were 30.01°, 45.05° and 89.92°. The deviations from the expected values are fully explained by uncertainties in the experimental methodology. Two curled papers were also measured. One with radius 38.79 mm (here called the paper with high magnitude of curl) and one with 81.28 mm (low magnitude of curl). Again it can be concluded that paper assumes approximately a cylindrical shape when it is subjected to humidity changes. It can be noted that a cylindrical model very well describes the paper with a high magnitude of curl. The error between the model and the measurements is in the same size as for the waste pipe measurements. The paper with low magnitude of curl, however, seemed to be skewed. Despite this most of the data points are within 1 mm from the model assumption.

Optical surface profile measurements combined with least squares fitting of a half-cylinder seems to be ideal for automated analysis of curl in paper. Such a system could warn the paper manufacturer when the paper quality has dropped below a certain limit by calculating the magnitude of curl, which is given as one number that easily can be compared to a limit value. If more data are needed in for instance research and development this method gives both the complete shape of the paper sheet and the residuals from the cylinder model.

REFERENCES

1. P. Glynn, W. Jones, and W. Gallay, "The fundamentals of curl in paper," *Pulp Paper Mag. Can.* (60), pp. T316–T323, 1959.
2. W. Gallay, "Stability of dimensions and form of papers," *Tappi J* (56), pp. 54–63, 1973.
3. T. Uesaka, I. Kodaka, S. Okushima, and R. Fukuchi, "History-dependent dimensional stability of paper," *Rheologica Acta* (28), pp. 238–245, 1989.
4. P. Viitaharju and K. Niskanen, "Chiral curl in thin papers," *J. Pulp Paper Sci.* (20), pp. J148–J152, 1994.

5. A. Nordström, P. Gudmundson, and L. Carlsson, "Influence of sheet dimensions on curl of paper," *J. Pulp Paper Sci.* (24), pp. 18–25, 1998.
6. P. Glynn and W. Gallay, "Further studies on the mechanism of curl in paper," *Pulp Paper Mag. Can.* (63), pp. T418–T424, 1962.
7. M. Hyer, "Some observations on the curved shape of thin unsymmetric laminates," *J. Compos. Mater.* (15), p. 318, 1981.
8. A. Nordström, L. Carlsson, and J.-E. Hägglund, "Measuring curl of thin papers," *Tappi J.* (80), pp. 238–244, 1997.
9. R. Brooks and L. Heflinger, "Moir gauging using optical interference patterns," *Appl. Opt.* (8), pp. 935–939, 1969.
10. G. Indebetouw, "Profile meaurements using projection of running fringes," *Appl. Opt.* (17), pp. 2930–2933, 1978.
11. M. Takeda and K. Mutoh, "Fourier transform profilometry for automatic measurements of 3-d object shape," *Appl. Opt.* (22), pp. 3977–3982, 1983.
12. V. Srinivasan, H. Liu, and M. Halioua, "Automated phase-measuring profilometry of 3-d diffuse objects," *Appl. Opt.* (23), pp. 3105–3108, 1984.
13. H. Saldner and J. Huntley, "Temporal phase unwrapping: application to surface profiling of discontinuous objects," *Appl. Opt.* (36), pp. 2770–2775, 1997.
14. M. Sjödahl and P. Synnergren, "Measurement of shape by using projected random patterns and temporal digital speckle photography," *Appl. Opt.* (38), pp. 1990–1997, 1999.
15. M. Sjödahl, "Electronic speckle photography: increased accuracy by nonintergral pixel shifting," *Appl. Opt.* (33), pp. 6667–6673, 1994.
16. P. Synnergren and M. Sjödahl, "A stereoscopic digital speckle photography system for 3-d displacement field measurements," *Opt. Lasers Engng.* (31), pp. 425–443, 1999.
17. Y. Bard, *Nonlinear Parameter Estimation*, Academic Press, New York, 1974.
18. Å. Björck, *Numerical Methods for Least Squares Problems*, SIAM, Philadelphia, 1996.
19. B. O'neill, *Elementary Differential Geometry*, Academic Press, Orlando, 1966.
20. M. Sjödahl, "Accuracy in electronic speckle photography," *Appl. Opt.* (36), pp. 2875–2885, 1997.
21. M. Gulliksson, I. Söderkvist, and P.-Å. Wedin, " Weighted Nonlinear Least Squares with Equality Constraints," *SIAM J. Optimization* **7**, pp. 208–224, 1997.